RESEARCH PAPER

ACTA PHYSIOLOGICA

Ion permeability profiles of renal paracellular channel-forming claudins

Ioanna Pouyiourou[1] | **Anja Fromm[1]** | **Jörg Piontek[1]** | **Rita Rosenthal[1]** | **Mikio Furuse[2,3,4]** | **Dorothee Günzel[1]**

[1]Clinical Physiology/Nutritional Medicine, Medical Department, Division of Gastroenterology, Infectiology, Rheumatology, Charité–Universitätsmedizin Berlin, Berlin, Germany

[2]Division of Cell Structure, National Institute for Physiological Sciences, Okazaki, Japan

[3]Physiological Sciences Program, Graduate Institute for Advanced Studies, SOKENDAI, Okazaki, Japan

[4]Nagoya University Graduate School of Medicine, Nagoya, Japan

Correspondence
Dorothee Günzel, Clinical Physiology/Nutritional Medicine, Medical Department, Division of Gastroenterology, Infectiology, Rheumatology, Charité–Universitätsmedizin Berlin, Berlin 12203, Germany.
Email: dorothee.guenzel@charite.de

Abstract

Aim: Members of the claudin protein family are the major constituents of tight junction strands and determine the permeability properties of the paracellular pathway. In the kidney, each nephron segment expresses a distinct subset of claudins that form either barriers against paracellular solute transport or charge- and size-selective paracellular channels. It was the aim of the present study to determine and compare the permeation properties of these renal paracellular ion channel-forming claudins.

Methods: MDCK II cells, in which the five major claudins had been knocked out (claudin quintupleKO), were stably transfected with individual mouse Cldn2, -4, -8, -10a, -10b, or -15, or with dog Cldn16 or -19, or with a combination of mouse Cldn4 and Cldn8, or dog Cldn16 and Cldn19. Permeation properties were investigated in the Ussing chamber and claudin interactions by FRET assays.

Results: Claudin-4 and -19 formed barriers against solute permeation. However, at low pH values and in the absence of HCO_3^-, claudin-4 conveyed a weak chloride and nitrate permeability. Claudin-8 needed claudin-4 for assembly into TJ strands and abolished this anion preference. Claudin-2, -10a, -10b, -15, -16+19 formed highly permeable channels with distinctive permeation profiles for different monovalent and divalent anions or cations, but barriers against the permeation of ions of opposite charge and of the paracellular tracer fluorescein.

Conclusion: Paracellular ion permeabilities along the nephron are strictly determined by claudin expression patterns. Paracellular channel-forming claudins are specific for certain ions and thus lower transepithelial resistance, yet form barriers against the transport of other solutes.

KEYWORDS
calcium, claudin protein family, Eisenman sequence, magnesium, nephron, paracellular ion channel, tight junction

Mikio Furuse and Dorothee Günzel contributed equally to this study.

1 | INTRODUCTION

Claudins are a family of tight junction (TJ) proteins that assemble into TJ strands and regulate paracellular transport across epithelia. Whereas all strand-forming claudins contribute to the barrier function of TJs and, for example, block permeation of molecules > ~200 Da and pathogens, some claudins, in addition, confer ion selectivity to the paracellular pathway (for reviews see, e.g., Refs. [1,2]). Segment-specific claudin expression patterns along the nephron were recognized immediately after the discovery of the first claudins.[3–5] Today, many recent studies employing modern sequencing techniques provide publicly available databases that allow to confirm and refine segmental claudin (Cldn) expression patterns (collection of data sets at http://humphreyslab.com/SingleCell/search.php, https://esbl.nhlbi.nih.gov/MRECA/Nephron/,[6] https://cello.shinyapps.io/kidneycellexplorer/[7]; for Cldn expression pattern extraction see, e.g., Refs. [2,8,9]).

Claudins expressed, at relevant levels, along the nephron, comprise Cldn1, -2, -3, -4, -7, -8, -10a, -10b, -12, -14 (Cldn14 expressed only when plasma Ca^{2+} levels are high[10–12]), -15, -16, and -19.[2,8,9] In addition, Cldn1 is expressed in the parietal cells of Bowman's capsule,[13] Cldn5 in podocytes,[8] and Cldn5 and -15 in renal endothelia.[5,8,14] Various studies, by claudin overexpression in different epithelial cell lines or by claudin knockout in mice, indicate that of these claudins, Cldn1, -3, -5, -14, and -19 form barriers against paracellular ion transport (e.g., Refs. [15–21]). In contrast, Cldn10a has been found to convey paracellular anion permeability to the paracellular pathway.[22,23] Cldn2,[24] -10b,[25] -12,[26,27] -15,[28] and the combination of Cldn16+19[29,30] have been reported to act as paracellular cation channels, but with different permeabilities for mono- and divalent cations, respectively. For Cldn4, -7, and -8, the situation is less clear, they have been described as barrier-forming[31–35] or potentially channel-forming,[36–40] or contributing to channel formation, as Hou et al.[38] observed that Cldn4 acts as a paracellular anion channel, but to assemble into TJ strands, has to interact with Cldn8.

To investigate the physiological properties of individual claudins, claudins have been overexpressed in various epithelial cell lines or knocked out in cell lines or mice, resulting in alterations in transepithelial resistance (TER) and permeabilities for ions (P_{ion}) or paracellular tracers (P_{tracer}) measured. However, results from such approaches may be affected by alterations in the expression or localization of endogenous claudins within these cell lines. One example is the replacement of endogenous Cldn2 by exogenous Cldn8 in MDCK II, causing a decrease in paracellular P_{Na}.[41]

Recently, MDCK II claudin quintuple knockout (claudin quinKO) cells were developed, a MDCK II-derived cell line, in which the five major, strand-forming claudins, Cldn1, -2, -3, -4, and -7 were knocked out.[33,42] Two further endogenous claudins, Cldn12 and Cldn16, are still expressed, however, these claudins do not form strands even if exogenously overexpressed in these cells.[33] Claudin quinKO cells still express ZO-1, ZO-2, Ocln, and JamA. Despite the absence of TJ strands, the paracellular cleft in claudin quinKO cells maintained a width of about 6–7 nm, and the paracellular movement of larger molecules (dextrans with a molecular weight of ≥4 kD) was restricted. This restriction was removed, if, in addition to the claudins, JamA was knocked out.[42]

Overexpression of Cldn1, -3, -4, and -7 resulted in TJ-formation and TER values of several thousand $\Omega\,cm^2$.[33] In contrast, overexpression of Cldn2, -10b, and -10a resulted in TJs with strong cation preference (Cldn2 and Cldn10b) or anion preference (Cldn10a).[33]

It was the aim of the present study to utilize claudin quinKO cells to overexpress and investigate the individual ion permeability profiles of all potentially paracellular channel-forming claudins expressed in the kidney: Cldn2, -10a, -10b, -15, Cldn19 in the presence and absence of Cldn16, and Cldn4 in the presence and absence of Cldn8. Only Cldn12 had to be omitted, as it did not form TJs under the present conditions.

2 | RESULTS

2.1 | Ion permeability of transfected claudin quinKO cell layers

Electrical properties of claudin quinKO cell layers stably transfected with mouse Cldn2, -4, -8, -10a, -10b, or -15, or dog Cldn16 or -19 (equivalent to human CLDN19 isoform b), or doubly transfected with mouse Cldn4 and Cldn8 (Cldn4+8), or dog Cldn16 and Cldn19 (Cldn16+19) were investigated in Ussing chambers. Non-transfected and empty vector-transfected claudin quinKO cell layers served as negative controls. TER values of these cell layers are depicted in Figure 1A (see also Table S1). With the exception of Cldn8 and Cldn16 expressing cell layers, all cell layers had increased TER values compared to the negative controls.

As this indicated that at least some of the cell layers formed paracellular barriers, fluorescein (uranine, molecular weight 332 Da) was utilized as a paracellular tracer, and fluorescein permeability (P_{Fluo}) was determined by flux measurements (Figure 1B). Despite the fact that TER was only increased by a factor of about 2 in Cldn2, -10a, -10b, and -15 overexpressing cell layers, compared to negative controls, P_{Fluo} was reduced by more than a factor of 10 in these cell layers. In contrast, Cldn8 and -16 transfected cell layers had a similar P_{Fluo} as negative controls (Figure 1B). Thus, all claudins except Cldn8 and -16
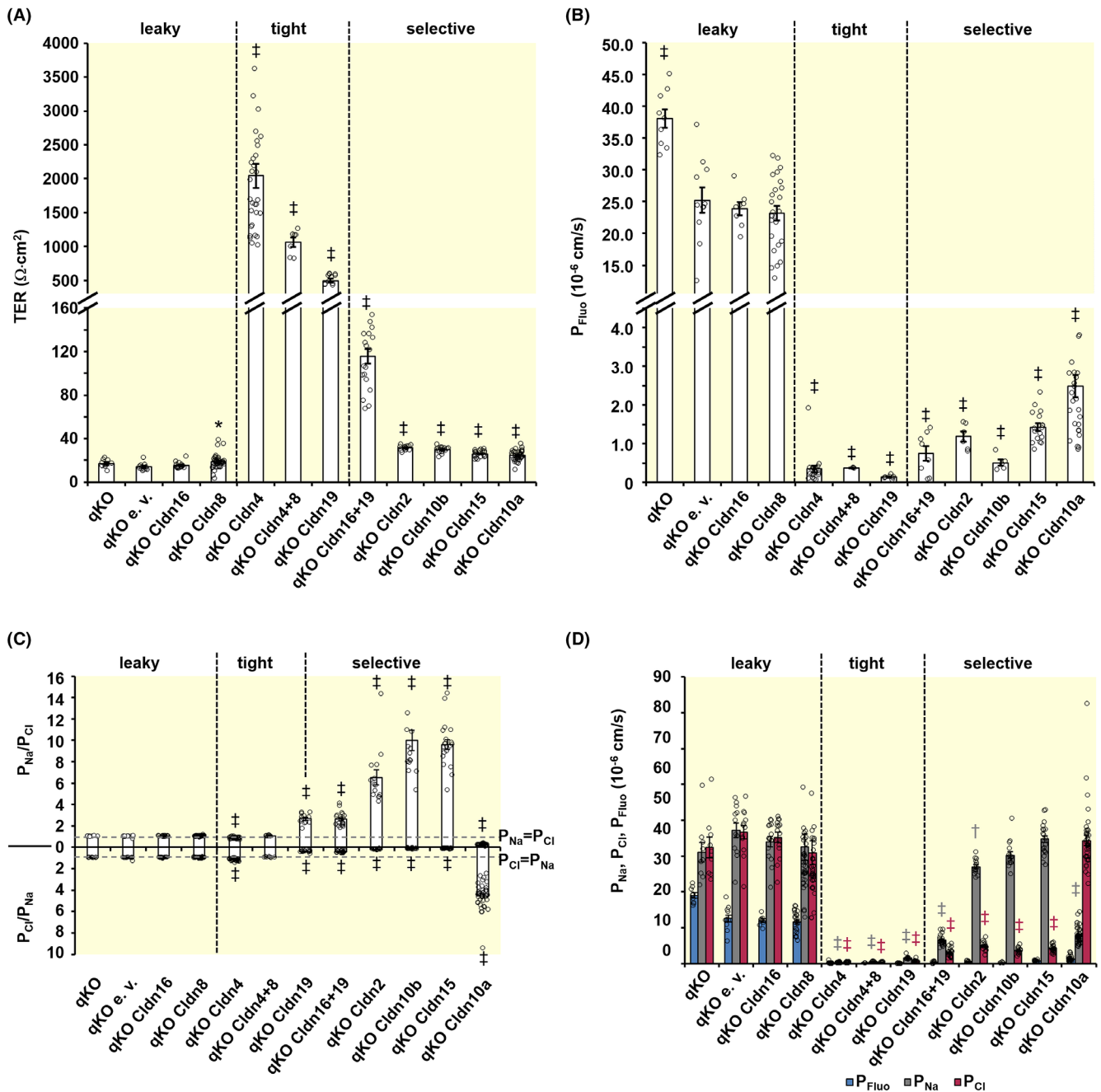
FIGURE 1 Barrier and channel properties of claudin quinKO (qKO) cell layers. Claudin quinKO cells were stably transfected with mouse (Cldn2, -4, -8, -10a, -10b, -15) or dog (Cldn16, -19) claudins or with the empty vector (e. v.) and barrier and channel properties were analyzed by Ussing chamber measurements. (A) TER values, (B) fluorescein permeability P_{Fluo} determined by flux measurements, (C) permeability ratios of Na^+ and Cl^- (P_{Na}/P_{Cl}, P_{Cl}/P_{Na}), determined by dilution potential measurement, (D) comparison of absolute permeabilities P_{Na}, P_{Cl}, and P_{Fluo}. For means ± SEM and n see Table S1. *$p < 0.05$; †$p < 0.01$; ‡$p < 0.001$; Brown-Forsythe and Welch ANOVA followed by Dunnet's T3 multiple comparisons test against empty vector-transfected controls.

were able to form efficient barriers against fluorescein permeation.

Dilution potential measurements demonstrated that Na^+ and Cl^- permeabilities were equal, that is, $P_{Na}/P_{Cl} = 1$, for negative controls, and also for cell layers transfected with Cldn8, Cldn4+8, and Cldn16. Cell layers transfected with Cldn2, -10b, and -15, had $P_{Na}/P_{Cl} \gg 1$,

cell layers transfected with Cldn19 and Cldn16+19 $P_{Na}/P_{Cl} > 1$, cell layers transfected with Cldn10a $P_{Na}/P_{Cl} \ll 1$, and cell layers transfected with Cldn4 $P_{Na}/P_{Cl} \leq 1$ (Figure 1C).

Using P_{Na}/P_{Cl} and TER values, the Kimizuka-Koketsu equation was employed to calculate absolute P_{Na} and P_{Cl} values.[25,43,44] In Cldn2, -10b, or -15 transfected cell layers,

P_{Na} reached approximately the same values as those for negative controls and Cldn8 or Cldn16-transfected cell layers, indicating, that Na^+ permeation was almost unrestricted. Analogously, in Cldn10a-transfected cells, P_{Cl} reached about the same value as those of the negative controls. Cldn4- and Cldn19-transfected cell layers formed efficient barriers against the permeation of Na^+ and Cl^-. P_{Na} of Cldn16+19 transfected cell layers was about a factor of 6 higher than that of Cldn19 transfected cells. P_{Cl} of Cldn2, -10b, -15 and -16+19-transfected cell layers and P_{Na} of Cldn10a-transfected cell layers, was low, yet still higher than the respective values of Cldn4- and Cldn19-transfected cell layers (Figure 1D). Under all conditions, P_{Na} and P_{Cl} were higher than P_{Fluo} of the respective cell layers (Figure 1D).

2.2 | Integration of Cldn8 and Cldn16 into TJ strands

To investigate why Cldn8 and Cldn16 did not increase TER of transfected cell layers, immunofluorescence (IF) staining and confocal laser scanning microscopy were employed to verify that Cldn8 and Cldn16 were overexpressed in claudin quinKO cells. Figure 2A,B demonstrates that both claudins are recruited to the junctional region. However, freeze-fracture electron microscopy (ffEM) revealed that these claudins did not form continuous TJ strands, but only punctual aggregates (Figure 2C,D). In contrast, Cldn4 and Cldn19 both showed strong junctional localization in IF staining (Figure 2A,B). IF staining further revealed that Cldn19 was able to recruit endogenous Cldn16 into TJs (Figure 2B). In ffEM, Cldn4 formed compact, mostly linear strands, whereas Cldn19 assembled into a loose network of strands with single strands extending far into the lateral membrane (Figure 2C,D). Co-transfection of Cldn4 and Cldn8 caused Cldn8 to strongly enrich in the cell–cell contacts (Figure 2A). Similarly, co-transfection of Cldn16 and Cldn19 caused a strong enrichment of Cldn16 in the junctional region (Figure 2B). In ffEM, the strand pattern of Cldn4 together with Cldn8 showed wider loops compared to Cldn4 alone (Figure 2C), whereas Cldn16 overexpression strongly reduced the lateral extension of Cldn19 (Figure 2D).

2.3 | Cation channel-forming claudins: Cldn2, Cldn10b, Cldn15, Cldn16+19

Bi-ionic potential measurements were employed to further investigate the permeability properties of the cation-selective claudins identified in Figure 1C. Permeabilities for alkali metal ions (Li^+, Na^+, K^+, Rb^+, Cs^+) showed distinct patterns: $P_{Na} > P_{Li} > P_K > P_{Rb} > P_{Cs}$, corresponding to Eisenman sequence X for Cldn10b transfected cell layers, $P_K \approx P_{Na} \geq P_{Li} > P_{Rb} > P_{Cs}$ corresponding to Eisenman sequence IX for Cldn2- and Cldn16+19-transfected cell layers, and $P_K \approx P_{Rb} \approx P_{Cs} > P_{Na} > P_{Li}$ corresponding to Eisenman sequence I to IV for Cldn15-transfected cell layers (Figure 3).

Permeability for Mg^{2+} and Ca^{2+} (P_{Mg}, P_{Ca}) differed markedly from P_{Na} in the investigated cell layers transfected with cation-selective claudins (Figure 4). Ca^{2+} permeation was almost unrestricted in Cldn16+19- and Cldn2-transfected cell layers and low in Cldn19-transfected cell layers. In Cldn10b- and Cldn15-transfected cell layers, P_{Ca} was considerably lower than in Cldn16+19- and Cldn2-transfected cell layers, yet higher than in Cldn19-transfected cell layers. In contrast, P_{Mg} was high in Cldn16+19-transfected cell layers (though less than P_{Ca}), but low in Cldn2-transfected cell layers and at a similar level as in Cldn10b- and Cldn15-transfected cell layers. As observed for P_{Ca}, P_{Mg} was lowest in Cldn19-transfected cell layers.

Similar to the Eisenman sequences for alkali metal ions, permeability patterns (Sherry sequences[45]) for earth alkali metal ions (Mg^{2+}, Ca^{2+}, Sr^{2+}, Ba^{2+}) differed for the different cell layers: Sherry sequence III for Cldn2-, Cldn19- and Cldn16+19-transfected cell layers ($P_{Ca} \geq P_{Ba} \approx P_{Sr} > P_{Mg}$) and Sherry sequence VII for Cldn10b- and Cldn15-transfected cell layers ($P_{Mg} > P_{Ca} \approx P_{Sr} \approx P_{Ba}$; Figure 4).

To estimate the pore size of the paracellular cation channels, bi-ionic potentials for NH_4^+, methylammonium$^+$ (MA), dimethylammonium$^+$ (DA), and in Cldn15-transfected cell layers, for tetramethylammonium$^+$ (TMA) were determined. Absolute permeabilities indicated that the pore size of Cldn10b is the smallest, as $P_{Na} > P_{NH4} > P_{MA} > P_{DA}$. Pore size for Cldn2 and Cldn16+19 are somewhat larger ($P_{NH4} \geq P_{Na} > P_{MA} > P_{DA}$) and largest for Cldn15 ($P_{NH4} \approx P_{Na} \approx P_{MA} > P_{DA} > P_{TMA}$). For non-transfected claudin quinKO cells, $P_{NH4} \approx P_{Na} \approx P_{MA} \approx P_{DA}$, that is, the paracellular flux even of DA appeared practically unrestricted. Interestingly, for Cldn16-transfected cell layers, P_{DA} was lower than P_{NH4}, P_{Na}, and P_{MA} ($P_{NH4} \approx P_{Na} \approx P_{MA} > P_{DA}$), though not as low as for Cldn15. Thus, even though Cldn16 did not form any obvious intercellular TJ strands,[33] its presence had a mild effect on the size selectivity of the paracellular pathway (Figure 5).

Pore diameters of cation pores can be estimated by plotting the square root (SQRT) of the permeability of the ammonium derivatives relative to that of Na^+ (P_x/P_{Na}) against the ionic diameters of NH4$^+$, MA$^+$, DA$^+$, and TMA$^+$, respectively.[46,47]

As shown in Figure 6A, this plot resulted in a straight line for Cldn10b-transfected cell layers, when assuming the NH_4^+ diameter of 2.96 Å given by Nightingale,[48]
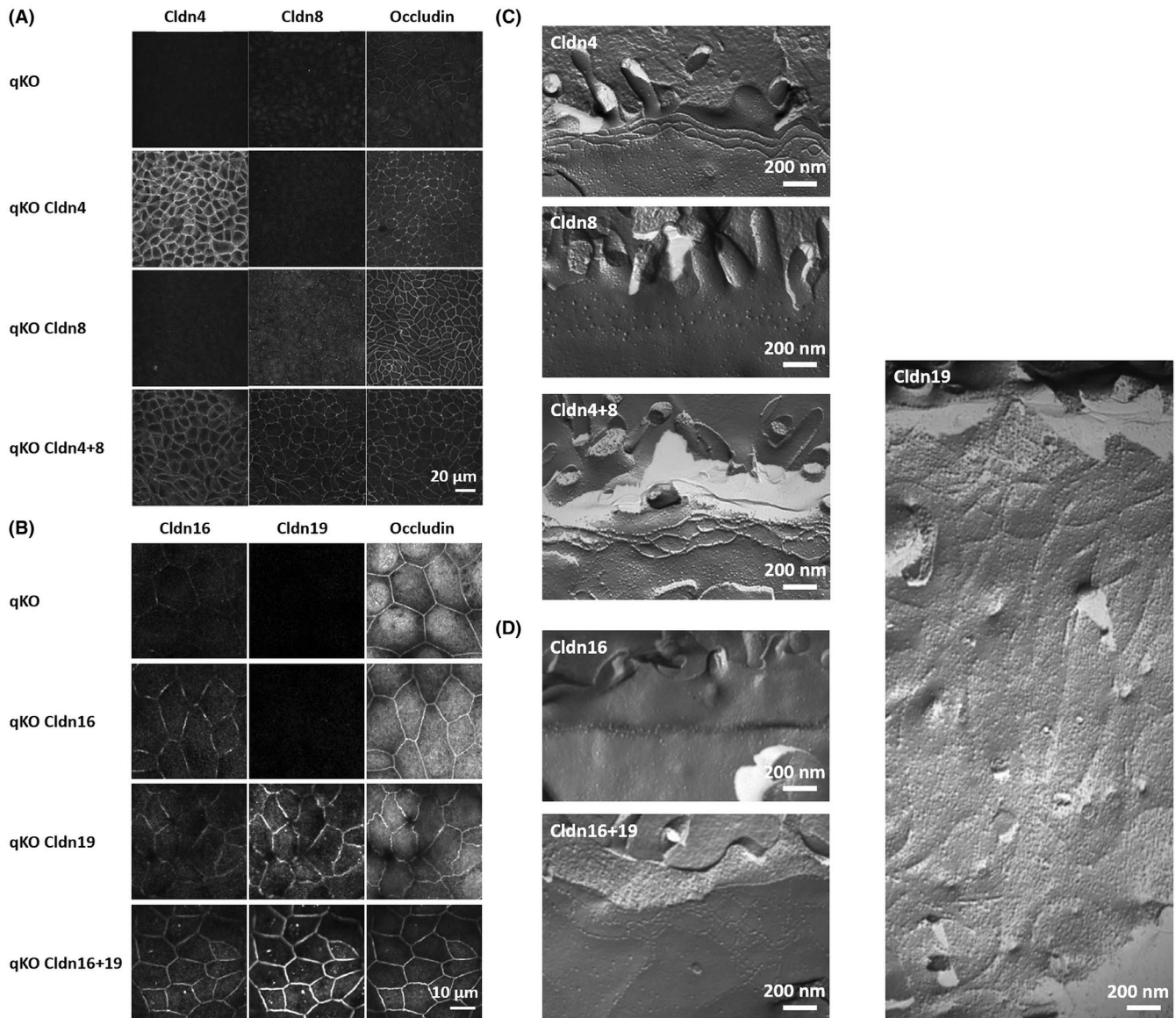
FIGURE 2 Immunofluorescence staining and freeze-fracture electron microscopy of transfected claudin quinKO (qKO) cell layers. (A) Immunofluorescence staining of claudin quinKO cells stably transfected with mouse Cldn4 showed strong junctional Cldn4 localization (co-localization with the TJ marker occludin), whereas Cldn8 was barely visible in the TJs of cell layers transfected with Cldn8. In contrast, both claudins co-localized with occludin, when co-transfected into claudin quinKO cells. (B) Immunofluorescence staining of claudin quinKO cells showed weak signals of endogenous Cldn16. Overexpression of Cldn16 resulted in discontinuous Cldn16-signals co-localizing with occludin. Overexpression of Cldn19 did not only result in junctional Cldn19 staining, but also recruiting endogenous Cldn16 to the junction. Upon co-transfection of Cldn16+19, both claudins showed strong co-localization within the TJ. (C) Freeze-fracture electronmicrographs of Cldn4-transfected claudin quinKO cell layers displayed predominantly continuous, parallel TJ strands. In contrast, Cldn8 did not form any strands but only widely spaced single particles, a pattern that precludes the formation of a tight barrier. Upon Cldn4+8 co-transfection, TJ strands had a particle-like appearance and formed more rounded meshes. (D) Similar to Cldn8-transfected cell layers and in agreement with the lack of a tight barrier, freeze-fracture electronmicrographs of Cldn16-transfected claudin quinKO cell layers did not display any continuous strands, but only spaced, single particles. Cldn19 formed a meshwork of strands at the apical pole of the cells, but single strands extended along the lateral membrane. When co-transfected, strands formed by Cldn16+19 displayed a more compact meshwork with only a few lateral strands.

and the diameters for MA^+ (3.78 Å), DA^+ (4.58 Å) and TMA^+ (5.5 Å) given by Villarroel et al.[49] Extrapolation to the intercept with the x-axis indicated a pore diameter of 4.9 Å. Extrapolating to the intercept with $SQRT(P_x/$ $P_{Na})=1$ suggests that the diameter of the Na^+ ion passing the pore is about 2.7 Å which is close to the fully unhydrated Na^+ diameter (1.9 Å[48]). For Cldn2-, −15-, −16+19-transfected cell layers no straight lines were
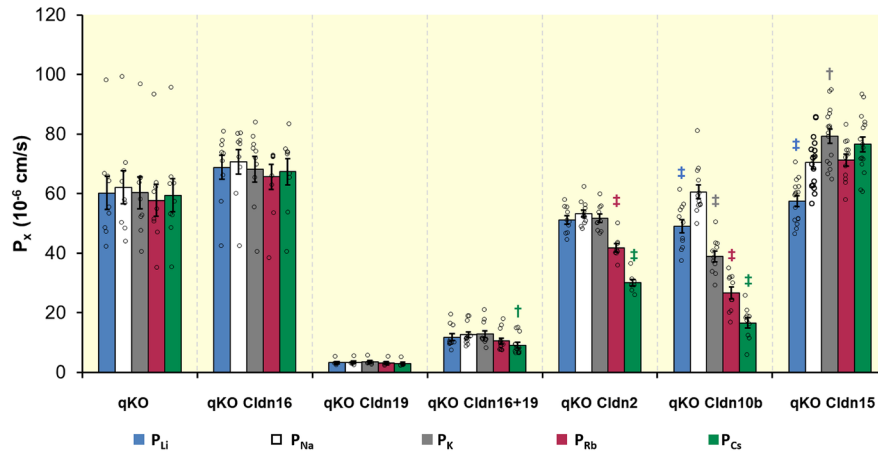
FIGURE 3 Permeabilities (P_X) of stably transfected claudin quinKO cell layers for monovalent cations (alkali metal ions Li$^+$, blue; Na$^+$, white; K$^+$, gray; Rb$^+$, red; Cs$^+$, green). Permeabilities of non-transfected control cells (qKO) and claudin quinKO cells stably transfected with claudins involved in paracellular cation transport were determined by bi-ionic potential measurements in the Ussing chamber. For means $\pm$ SEM and number of replicates n see Table S1. $^†p < 0.01$; $^‡p < 0.001$. One-way ANOVA and Dunnet's T3 multiple comparisons test against P_{Na} within each group.
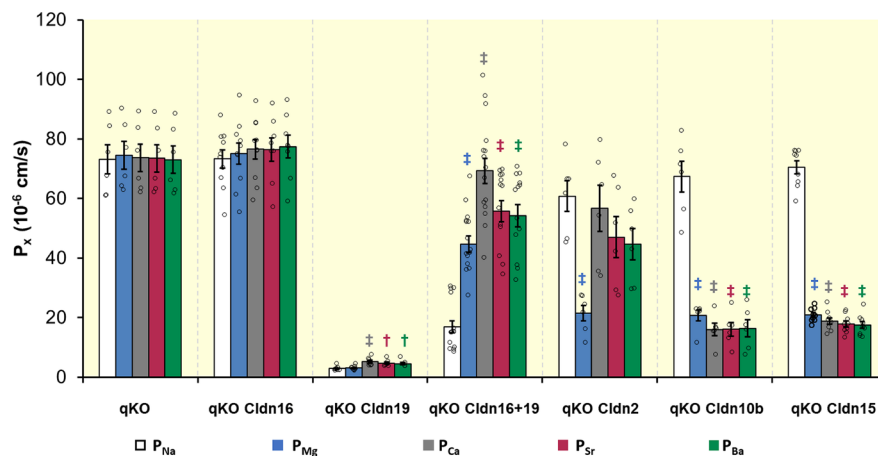

FIGURE 4 Permeabilities (P_X) of claudin quinKO cell layers for divalent cations (Mg^{2+}, blue; Ca^{2+}, gray; Sr^{2+}, red; Ba^{2+}, green) in comparison to P_{Na} (white). Permeabilities of non-transfected control cells (qKO) and claudin quinKO cells stably transfected with claudins involved in paracellular cation transport were determined by bi-ionic potential measurements in the Ussing chamber. For means $\pm$ SEM and number of replicates n see Table S1. $^†p < 0.01$; $^‡p < 0.001$. One-way ANOVA and Dunnet's T3 multiple comparisons test against P_{Na} within each group.

obtained when using the unhydrated NH$_4^+$ diameter given by Nightingale[48]; gray lines in Figure 6A. However, when assuming NH$_4^+$ diameter of 3.3 Å (Figure 6B), as given by Villarroel et al.[49], values fell on a straight line for Cldn2- and Cldn16+19-based channels, likely indicating that NH$_4^+$ passes the pore partially hydrated. Under these conditions, extrapolation to the intercept with the x-axis indicated that the pore diameter of Cldn2-based channels is about 5 Å and thus similar to Cldn10b-based channels. The pore diameter of Cldn16+19-based channels appeared to be about 5.8 Å. For Cldn15-based channels, even under these conditions, no straight line was

obtained. Therefore, NH$_4^+$ permeability was not used to estimate the Cldn15 pore size, but rather the permeability of the larger TMA, and a pore size of about 6.7 Å estimated.

2.4 | Putative anion channel-forming claudins: Cldn10a, Cldn4, Cldn4+8

As shown in Figure 1, Cldn4-, Cldn4+8-, and Cldn10a-transfected cell layers were able to restrict the paracellular passage of fluorescein, whereas Cldn8-transfected
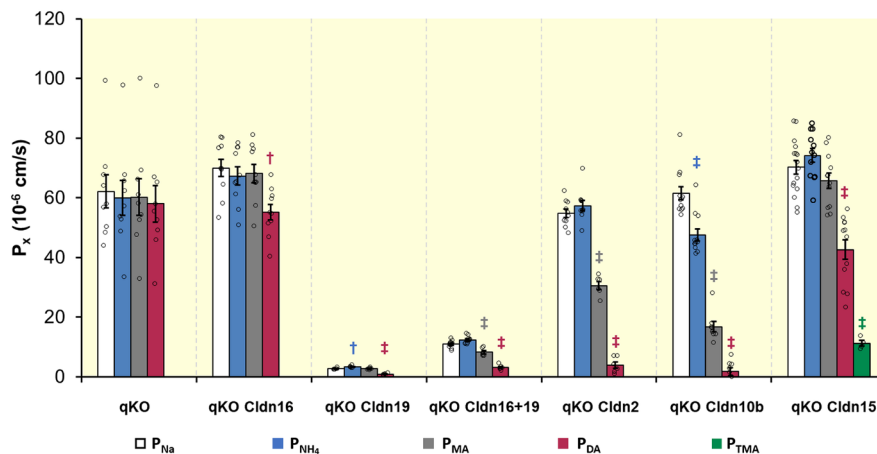
FIGURE 5 Permeabilities (P_X) of claudin quinKO cell layers for NH_4^+ (blue), methylammonium$^+$ (MA, gray), dimethylammonium$^+$ (DA, red), and tetramethylammonium$^+$ (TMA, green) in comparison to P_{Na} (white). Permeabilities of non-transfected control cells (qKO) and claudin quinKO cells stably transfected with claudins involved in paracellular cation transport were determined by bi-ionic potential measurements in the Ussing chamber. For means ± SEM and number of replicates n see Table S1. $^†p < 0.01$; $^‡p < 0.001$. One-way ANOVA and Dunnet's T3 multiple comparisons test against P_{Na} within each group.
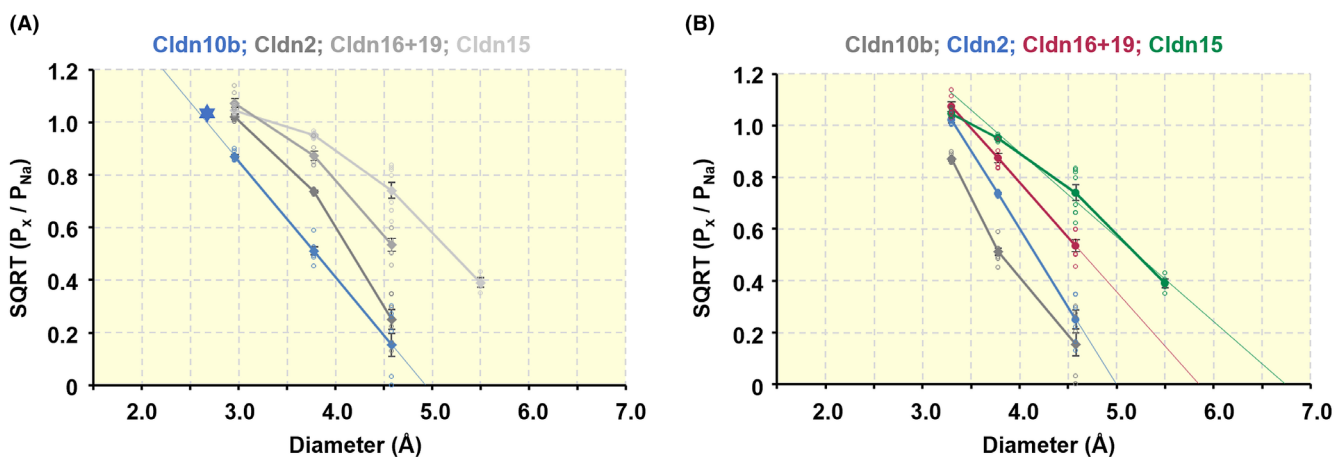

FIGURE 6 Pore size estimation of cation channel-forming claudins. Pore size was estimated as described by Yu et al.[46], assuming diameters of 3.78, 4.58, and 5.5 Å for methylammonium$^+$, dimethylammonium$^+$, and tetramethylammonium$^+$, respectively.[49] According to the Renkin Equation,[47] the square root of the relative permeabilities of ammonium derivatives (P_x/P_{Na}) should depend linearly on the diameter of these cations. The extrapolated intercept with the x-axis by linear regression indicates the pore size. (A) Estimation of the pore size for Cldn10b (blue), assuming the NH_4^+ diameter of 2.96 Å given by Nightingale.[48] The intercept with the x-axis indicates a pore diameter of 4.9 Å, and the * indicates the intercept with $P_x/P_{Na} = 1$. From this, the effective diameter of Na$^+$ is estimated to be ~2.6 Å, indicating that Na$^+$ is almost fully dehydrated while passing the pore of the Cldn10b-based channel. For Cldn2, Cldn16+19, and Cldn15 (gray), no straight lines were obtained. (B) Estimation of the pore size of Cldn2 (blue)-, Cldn16+19 (red)-, and Cldn15 (green)-based channels, assuming the NH_4^+ diameter of 3.3 Å given by Villarroel et al.[49] The intercepts with the x-axis indicate pore diameters of 5.0, 5.8, and 6.7 Å for Cldn2, Cldn16+19, and Cldn15, respectively. For Cldn10b (gray), no straight line was obtained.

cell layers were not. Initial experiments showed that TER values for Cldn8- and Cldn10a-transfected cell layers were always low, whereas TER values for Cldn4- and Cldn4+8-transfected cell layers declined with increasing number of passages. This decrease in TER was paralleled by an increase in P_{Fluo}, indicating a loss of TJ integrity (Figure S1A). Western blots confirmed a considerable loss of claudin expression in Cldn4- and Cldn8-expressing cell layers already after passage 2 (Figure S1B,C). In Cldn4+8-expressing cells, expression was more stable between passages 2 and 4, but more variable between individual cell layers from one passage. As it had been reported in the literature that Cldn4 phosphorylation might interfere with strand assembly, an antibody against phospho-Tyr 208-Cldn4 was employed. As shown in Figure S1D, signal strength for phospho-Tyr 208-Cldn4 did not increase with

higher passages, but simply paralleled that of the total Cldn4.

In contrast to P_{Fluo}, the relative Cl^- permeability, P_{Cl}/P_{Na}, in Cldn4-expressing cell layers did not increase but decreased with decreasing TER, reaching values of about 1 at TER values below about $700\,\Omega\cdot cm^2$ (Figure 7A). At higher TER values, P_{Cl}/P_{Na} in Cldn4-expressing cell layers was slightly, but consistently higher than that of Cldn4+8-expressing cell layers. The stronger anion selectivity was particularly evident when a TER interval was selected ($700–2000\,\Omega\cdot cm^2$; red dashed lines in Figure 7A, for mean values, see Table S2) in which a comparable number of data points were available for both types of cell layers.

Properties of Cldn10a were as expected for an anion channel-forming claudin. TER was low, but, compared to cell layers without functional TJs (Cldn8- or empty vector-transfected cell layers), P_{Fluo} was considerably lower (Figure S1A) and P_{Cl}/P_{Na} distinctly higher (Figure 7A).

To investigate anion permeability profiles of the putative paracellular anion channel-forming claudins, permeabilities for NO_3^-, HCO_3^-, $H_2PO_4^-$, and HPO_4^{2-} were investigated and compared to Cl^- permeability. To discriminate between the two physiologically relevant ionic forms of phosphate, $H_2PO_4^-$ and HPO_4^{2-}, bi-ionic potential measurements were carried out at pH 6 and pH 8.4. These solutions were HCO_3^--free and buffered with MES and TAPS, respectively. To test, whether the omission of

HCO_3^- had any effect on anion permeability, comparative experiments were conducted at pH 7.4, using HCO_3^--containing solutions, equilibrated with carbogen (95% O_2/5% CO_2), and HEPES-buffered, HCO_3^--free solutions equilibrated with 100% O_2 instead of carbogen. Whereas P_{Cl}/P_{Na} was not affected by the omission of HCO_3^- in any of the cell types (filled vs. open symbols in Figure 7A), P_{NO3}/P_{Na} was substantially increased in Cldn4-transfected cell layers at TER values $>700\,\Omega\cdot cm^2$ (red, filled symbols in Figure 7B). Again, for better comparison, a TER interval was selected ($700–2000\,\Omega\cdot cm^2$; red dashed lines in Figure 7B, for mean values, see Table S2) in which similar numbers of data points were available for both types of cell layers.

Because of the TER-dependence of the Cldn4-mediated effects, further experiments were restricted to Cldn4-transfected cell layers with TER values $>1000\,\Omega\cdot cm^2$ and Cldn4+8-transfected cell layers with TER values $>500\,\Omega\cdot cm^2$, to ensure sufficient Cldn4 and Cldn8 expression.

The increase in P_{NO3}/P_{Na} in the absence of HCO_3^- in Cldn4-transfected cell layers led to the hypothesis that Cldn4 might form paracellular channels that are permeable to HCO_3^-. However, P_{HCO3}/P_{Na} was «P_{Cl}/P_{Na} for Cldn4 and Cldn10a (Figure 8A). In Cldn4-transfected cell layers, P_{NO3}/P_{Na} was higher than P_{Cl}/P_{Na} even in the presence of HCO_3^-, whereas this was not the case in Cldn10a-transfected cells (Figure 8A). P_{NO3}/P_{Cl} and P_{HCO3}/P_{Cl} were both lower in Cldn10a-transfected cell
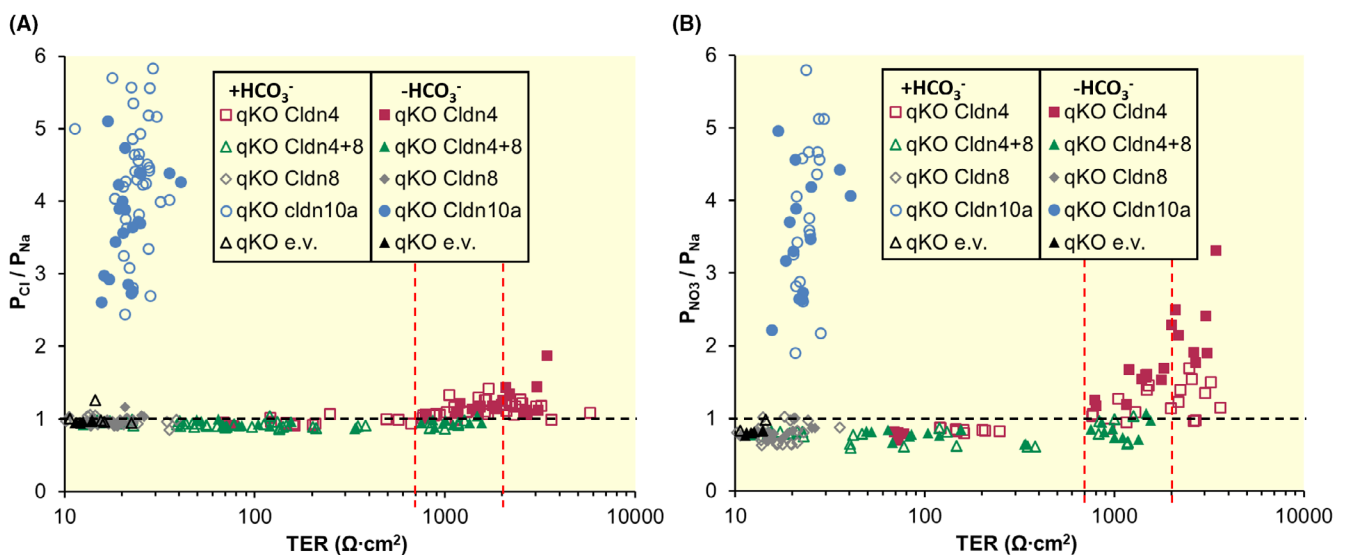
FIGURE 7 Permeability ratios P_{Cl}/P_{Na} (A) and P_{NO3}/P_{Na} (B) plotted against the corresponding TER values in claudin quinKO cells transfected with the empty vector (qKO e.v.) or putative anion channel-forming claudins. Bi-ionic potential measurements were performed in the Ussing chamber in CO_2/HCO_3^--buffered (open symbols) and CO_2/HCO_3^--free solutions (filled symbols). Red dashed lines, TER interval of $700–2000\,\Omega\cdot cm^2$ for better comparison of permeability ratios obtained from Cldn4- and Cldn4+8-transfected cell layers. Cell layers within this interval were from cell passages 2 or 3, Cldn4- and Cldn4+8-transfected cell layers with TER values below $700\,\Omega\cdot cm^2$ from passage ≥3. For mean permeabilities within this interval, see Table S2.

FIGURE 8 Anion permeabilities in CO_2/HCO_3^--buffered and CO_2/HCO_3^--free solutions. (A, B) Anion permeabilities (P_{Cl}, P_{HCO3}, P_{NO3}) relative to P_{Na} (A) or P_{Cl} (B) in Cldn4- and Cldn10a-transfect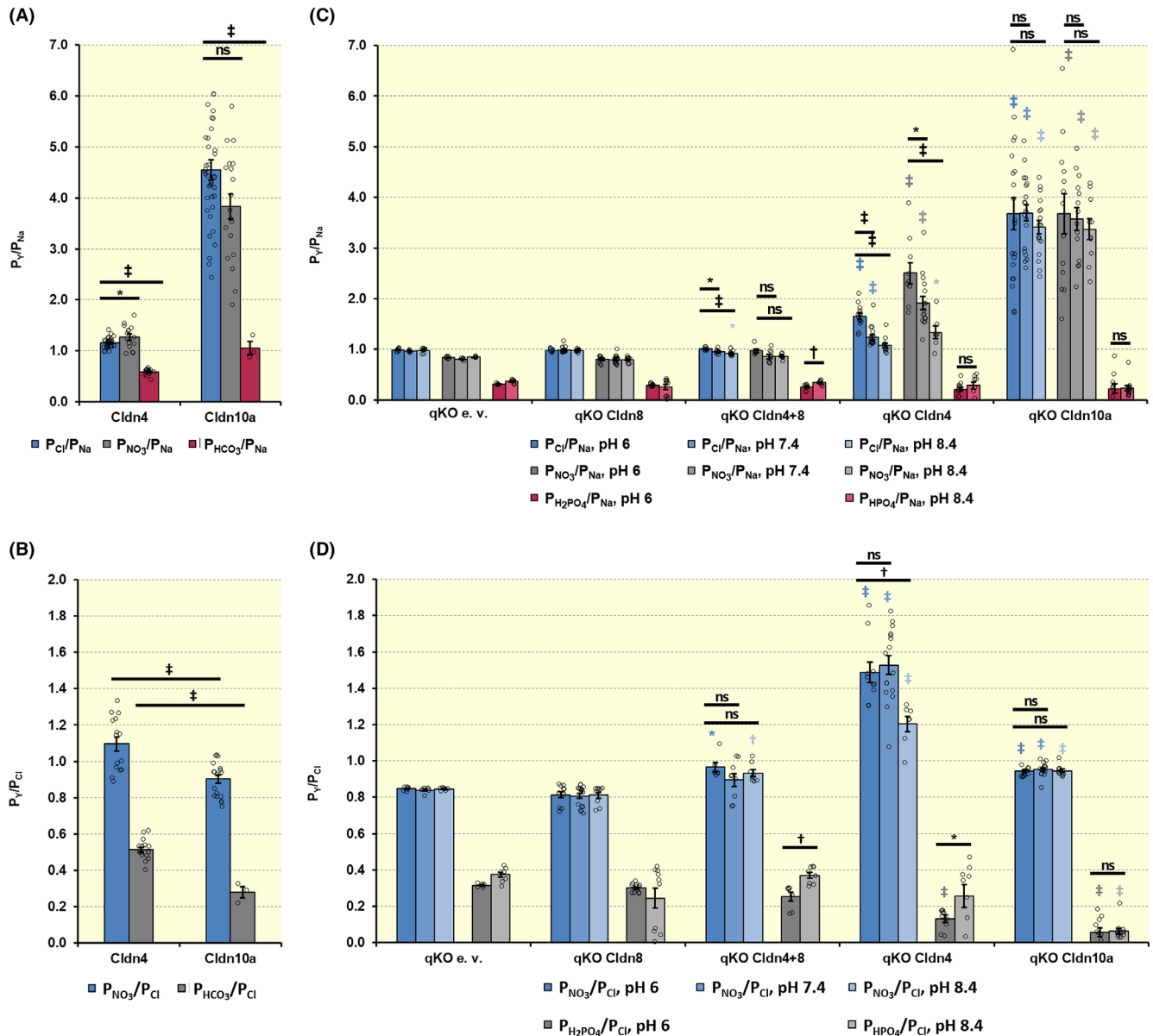ed claudin quinKO cells, measured in CO_2/HCO_3^--buffered solutions. (C, D) Anion permeabilities (P_{Cl}, P_{NO3}, P_{H2PO4}, P_{HPO4}) relative to P_{Na} (C) or P_{Cl} (D), measured in CO_2/HCO_3^--free solutions under acidic (pH 6), physiologic (pH 7.4) and alkaline conditions (pH 8.4) conditions. For means $\pm$ SEM and number of replicates n see Table S1. ns, not significant; $*p < 0.05$; $^\dagger p < 0.01$; $^\ddagger p < 0.001$. (A) one-way ANOVA and Dunnet's T3 multiple comparisons test; (B) Students t-test; C and D, colored symbols denote testing against empty vector-transfected controls (qKO e.v.; Brown-Forsythe and Welch ANOVA followed by a Dunnet's T3 multiple comparisons test), black symbols refer to testing of values obtained at pH 7.4 and pH 8.4 vs. pH 6 (Students t-test for phosphate, one-way ANOVA and Dunnet's T3 multiple comparisons test for Cl^- and NO_3^-).

layers compared to Cldn4-transfected cell layers, indicating a higher Cl^- specificity of Cldn10a compared to Cldn4 (Figure 8B).

In HCO_3^--free solutions P_{Cl}/P_{Na} and P_{NO3}/P_{Na} were increased in Cldn4- and Cldn10a-transfected cell layers compared to empty vector-transfected cells, whereas relative phosphate permeability was unaltered. P_{Cl}/P_{Na} and P_{NO3}/P_{Na} for Cldn4-transfected cell layers were both pH-dependent and considerably higher at acidic compared to

alkaline conditions. Cldn4+8-transfected cell layers similarly showed a pH dependence for P_{Cl}/P_{Na} but not P_{NO3}/P_{Na}. In addition, these cells displayed a slight preference for HPO_4^{2-} compared to $H_2PO_4^-$ (Figure 8C). At acidic pH, the effect may predominantly be due to a more efficient sealing against the permeation of Na^+, as P_{NO3}/P_{Cl} did not differ between pH 6 and pH 7.4 (Figure 8D). At pH 8.4, P_{NO3} was more strongly affected than P_{Cl} (P_{NO3}/P_{Cl} at pH 8.4 < P_{NO3}/P_{Cl} at pH 7.4, Figure 8D). Ion permeabilities

of Cldn10a-transfected cells did not show any significant pH dependence (Figure 8C,D).

All cell layers, including empty vector-transfected cell layers, displayed a low phosphate permeability, both relative to Na^+ and Cl^- (Figure 8C,D). This may indicate that not primarily claudins but other junctional components may be responsible for the regulation of paracellular phosphate permeability.

2.5 | FRET measurements

To determine, whether Cldn4 and Cldn8 were interacting within TJ strands, YFP (yellow fluorescent protein)- or CFP (cyan fluorescent protein)-tagged human CLDN4 and CLDN8 (hCLDN4, hCLDN8) were overexpressed in claudin quinKO cells, and FRET (Förster/fluorescence resonance energy transfer) determined by life cell imaging in a confocal microscope. Different ratios of the plasmids were employed for transfection to obtain different YFP/CFP ratios, as FRET of claudins within TJ strands is known to depend on this FRET acceptor/-donor ratio.[50] Signals were calibrated using a YFP/CFP tandem protein so that YFP/CFP ratios directly reflect the ratios of the claudins within the regions of interest.

As shown in Figure 9, within the YFP/CFP range of 1 to 5 (dashed blue lines in Figure 9), FRET efficiency of hCLDN8 was lower than that of hCLDN4. The

highest FRET efficiency was obtained for the interaction of hCLDN4 with hCLDN8. However, for the co-expression of the two claudins, the relationship between FRET efficiency and the YFP/CFP ratio did not show the expected saturation at high YFP/CFP, when, stochastically, each CFP (FRET donor) is neighboring the maximum possible number of YFP (FRET acceptor) molecules (for further explanation see Figure S2). Furthermore, it was almost impossible to obtain hCLDN8/hCLDN4 ratios >1 (i.e., green data points with YFP-hCLDN8/CFP-hCLDN4 > 1 or blue data points with YFP-hCLDN4/CFP-hCLDN8 < 1 in Figure 9). This indicates a preferred stoichiometry between hCLDN4 and hCLDN8, however, this needs to be studied in more detail in the future.

3 | DISCUSSION

Classical ion channels, which are embedded in lipid membranes, and paracellular, claudin-based channels within TJs differ fundamentally. Whereas in a lipid membrane, lipids form the barrier, and ion channels provide the pores that allow certain ions to pass through the lipid membrane barrier, claudins must form both the paracellular barrier against the unwanted passage of ions and molecules and the selective pores. In many previous studies investigating the properties of paracellular channel-forming claudins, cell lines with very high TER
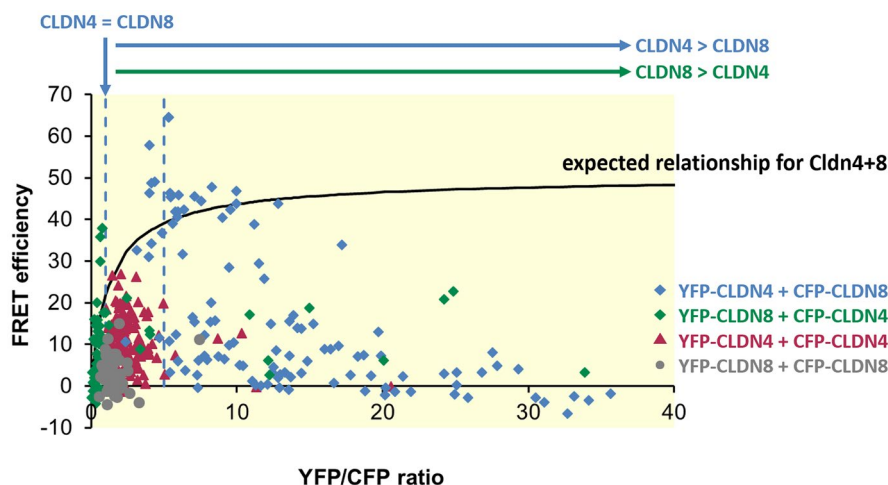
FIGURE 9 Analyses of the interaction of hCLDN4 and hCLDN8 within TJs by FRET (Förster/fluorescence resonance energy transfer). FRET of YFP- and CFP-tagged claudins within TJs has previously been demonstrated to increase with increasing YFP/CFP ratios and to reach saturation at high YFP/CFP ratios. Cell–cell contacts of claudin quinKO cells transiently co-transfected with YFP- and CFP-hCLDN8 showed low FRET efficiencies (gray symbols), indicating only weak interaction between hCLDN8 protomers, consistent with the observation that hCLDN8 alone was not able to form functional TJs. FRET efficiencies for YFP- and CFP-hCLDN4 (red symbols) were larger, in keeping with the ability of hCLDN4 to form high-resistance TJs. Combination of YFP-hCLDN4 with CFP-hCLDN8 (blue symbols) and YFP-hCLDN8 with CFP-hCLDN4 (green symbols), respectively, showed the highest FRET efficiencies for YFP-hCLDN4/CFP-hCLDN8 ratios between about 3 and 6. For YFP-hCLDN8/CFP-hCLDN4 highest FRET efficiencies were obtained between ratios of about 0.75 and 1, likely because at lower hCLDN8/hCLDN4 ratios the resulting low YFP/CFP ratio was unfavorable for FRET (for a detailed explanation of the expected relationship, see Figure S2).

values were used. In these cell lines, barrier-forming claudins fulfill the sealing function, and certain channel-forming claudins were specifically embedded in this matrix. In the present study, as in two recent studies,[33,51] the approach was reversed. The five main claudins of the MDCK II cells were knocked out and individual channel-forming claudins were overexpressed. By analogy, for corresponding studies on ion channels, all lipids would have to be replaced by densely packed ion channel proteins. Under these conditions, it is demonstrated (Figure 1B,D) that all channel-forming claudins form effective barriers against the small paracellular tracer fluorescein. They also form barriers against the ions of opposite charge of their preferred ions (Figure 1D).

Claudin quinKO cells used in the present study express low levels of endogenous Cldn12 and Cldn16. Previous experiments showed that these claudins were unable to form strands, even if exogenously overexpressed in claudin quinKO cells.[33] However, it has to be kept in mind that they may integrate into existing strands formed by overexpressing other claudins.

Of the claudins stably overexpressed in the current study, mCldn8 and dCldn16, were unable to form functional TJs: ffEM revealed punctate, discontinuous clusters, TER was similarly low, and P_{Fluo} similarly high as in non-transfected and empty vector-transfected cell layers. However, Cldn8 was able to insert into TJs formed by Cldn4 and Cldn16 into TJs formed by Cldn19.

The observation that FRET efficiency for junctional YFP-hCLDN4/CFP-hCLDN4 is larger than that for YFP-hCLDN8/CFP-hCLDN8, is an indication of a direct interaction of Cldn4 protomers within cell–cell contacts. In this respect, Cldn4 in quinKO cells behaves similarly to other strand-forming claudins (e.g., Cldn1, -3, -10b) in transfected HEK293 and MDCK C7 cells.[50,52] Additionally, mouse Cldn4 (mCldn4) as well as dog Cldn4 (dCldn4[33]) are able to form functional TJs, resulting in very high TER and very low P_{Fluo}. Strand formation was directly demonstrated for dCldn4 in a previous study, employing freeze-fracture electron microscopy,[33] whereas in other studies, formation of Cldn4-based TJ strands was not, or only infrequently observed.[51,53,54] Thus, Cldn4 has the ability to polymerize into TJ strands, even though this process appears to be more strongly dependent on the cellular context than for other strand-forming claudins.

The very high TER caused by Cldn4 overexpression in claudin quinKO cells, which was independent of the presence or absence of HCO_3^- and of extracellular pH (see Table S1) shows that Cldn4 is a barrier-forming and not a channel-forming claudin as previously suggested.[38,39] Yet, under certain conditions a slight preference for Cl^- was observed, that is, when forming a tight barrier (TER $> 700\,\Omega\cdot cm^2$) at low pH values, in the absence of

HCO_3^-. These are conditions that may physiologically be found in the medullary collecting duct of the mammalian kidney. However, due to the very low absolute P_{Cl} (Figure 1D), Cldn4 will not convey bulk paracellular Cl^- movement, as previously suggested for the collecting duct.[38] The Cl^- preference will, however, allow to establish and maintain a stable transepithelial voltage difference in the presence of a transepithelial Cl^- gradient, as, for example, observed in the renal connecting tubule and collecting duct.[55]

Whether the observed P_{NO3} may provide mechanistic information only or is of physiological relevance, is unclear. NO_3^- is enriched in salivary glands and secreted into saliva, and involvement of the basolateral anion transporter sialin in this process has been suggested.[56] Salivary glands also express high levels of Cldn4.[57] However, no data on saliva NO_3^- concentration in Cldn4 knockout animals are available.

Cldn8, when integrating into Cldn4-based TJ strands, contrary to previous findings,[38] appears to abolish the Cldn4-induced anion preference (Figures 1C, 7, and 8B,D). Cldn8 has been reported to be up-regulated by aldosterone,[32,58] in parallel with ENaC. In the collecting duct, this might diminish the lumen negative potential and thus facilitate Na^+ reabsorption.

FRET data indicate a stable integration of Cldn8 into Cldn4-based TJs. Interestingly, the highest FRET efficiencies were obtained at hCLDN4/hCLDN8 ratios of about 3 to 6. This would correspond to hCLDN8/hCLDN4 ratios of 0.17 to 0.33. Indeed, for YFP-hCLDN8/CFP-hCLDN4, highest FRET efficiencies were obtained at low ratios of about 0.6 and 0.8. At even lower hCLDN8/hCLDN4 ratios, FRET efficiency was lower, most likely because the resulting very low YFP/CFP ratio was unfavorable for FRET (for a detailed explanation of the expected relationship, see Figure S2). The distribution of the datapoints, that is, very few data points below hCLDN4/hCLDN8 = 3 (blue data points in Figure 9) and very few data points above hCLDN8/hCLDN4 = 1 (green data points in Figure 9) indicates that it may be impossible to force more hCLDN8 into hCLDN4-based strands than at a ratio of about 1:1. However, having even more than about 5 hCLDN4 for 1 hCLDN8 protomer lowers FRET and thus appears to inhibit the integration of hCLDN8 into hCLDN4-containing strands. This may be explained by competition between hCLDN4 and hCLDN8 protomers during the multistep polymerization into claudin strands.[59] In sum, the FRET data suggest thus a rather fixed stoichiometry of hCLDN8:hCLDN4 of ~1:2 to 1:4 in strands, but more studies are needed to further clarify stoichiometry and underlying mechanisms.

For the investigation of Cldn16 and Cldn19 in claudin quinKO cells two limitations were experienced. First, for

unknown reasons, mouse Cldn19 failed to reconstitute TJs in claudin quinKO cells, because of its intracellular accumulation. Therefore, cell clones stably expressing dog Cldn19 with or without dog Cldn16 were established. These cell clones generated functional tight junctions. Accordingly, the previously published claudin quinKO cells overexpressing dog Cldn16[33] were used for comparison in the current analyses. Second, the endogenous Cldn16 interfered with the study of pure Cldn19 properties in claudin quinKO cells overexpressing Cldn19. Similar to Cldn4, Cldn19 formed a strong paracellular barrier, however, this barrier exhibited a cation preference. This cation preference can be explained by the insertion of endogenous Cldn16. It is noteworthy that P_{Na}/P_{Cl} was equally increased in Cldn19 and Cldn16+19 transfected cell layers (P_{Na}/P_{Cl} of 2.7 ± 0.1, $n = 12$; 2.7 ± 0.2, $n = 19$; Figure 1C), indicating that there was only a difference in number of channels, not in channel properties. Nonetheless, for an isolated investigation of the Cldn19 properties, an additional knockout of Cldn16 would be desirable.

It has to be emphasized, however, that Cldn16+19 transfected claudin quinKO cells are the first cell culture system that shows the high P_{Ca} and P_{Mg} inferred for these two claudins since their discovery.[30,60,61] P_{Ca} and P_{Mg} are by a factor of 4.6 and 3.0, respectively, larger than P_{Na} (Figure 3) which makes Cldn16+19-based cation channels unique and, despite their modest preference of Na^+ over Cl^-, true channels for divalent cations. In contrast, for Cldn2-based channels, P_{Ca} and P_{Na} are equally high, but P_{Mg} low. Together, these findings explain, why Ca^{2+} reabsorption, but not Mg^{2+} reabsorption is high in the proximal tubule of the nephron, but both ions are reabsorbed in the thick ascending limb of Henle's loop (for review see Ref. [2]).

In contrast, P_{Na} is high, but P_{Ca} and P_{Mg} is low for the two other cation channel-forming claudins, Cldn10b and Cldn15. In summary, relative monovalent cation permeabilities found in the present study are similar to previously published results.[25,46,62] Eisenman and Sherry sequences confirm that Cldn10b is able to almost fully dehydrate the permeating cations. Cldn2 has a similar pore size as Cldn10b, but a lower ability to dehydrate small cations. Cldn15, in contrast, does not dehydrate the permeating cations (Eisenman sequence I). Cldn2 and Cldn-10b pore size estimates are smaller than those reported for these claudins overexpressed in MDCK C7 cells.[62] The reason is unknown but may be related to the presence of endogenous claudins.

For Cldn10a, its role as a paracellular Cl^- channel and its exclusion of HCO_3^- are confirmed in the present study.[22,25] The monovalent as well as the divalent form of phosphate are also excluded. In contrast to our previous study, no preference for NO_3^- over Cl^- was observed,[25]

possibly again due to interactions with endogenous claudins in the previous study.

3.1 | Sequence comparisons

All claudin subtypes for which channel formation was demonstrated experimentally, either reproducibly by several labs and unquestionably (Cldn2, -10a, -10b, -15, -16) or with clear experimental support (-12, -17, -21) show striking sequence differences compared to claudins that unquestionably form an ion barrier (Cldn1, -3, -5, (-7), -11, -14, -19; Figure S3).

Especially the barrier-forming classic claudins (Cldn1, -3, -5, (-7), -14, -19) contain the ECS1 "barrier" consensus sequence $Y/F/hx^{21}Q/hSTx^3Q/sC_{64}K/qV/M/i/lY/fD/r/e$ whereas classic cation channel-forming claudins (Cldn2, -10b, -15) contain the ECS1 "cation" consensus sequence $I/V/Yx^{20-21}D/hST/Lx^3N/q/sC_{64}D/K/W/rD/I/EF/yP/s$ and the classic anion channel-forming claudins (Cldn10a, -17) the ECS1 "anion" consensus sequence $R/F/x^{20-21}N/QAL/M/k/rx^3H/QC_{64}K/RF/PH/YF/n/s$ (Figure S3).

Cldn4 belongs to the classic claudins,[63] and clearly contains the ECS1 consensus sequence of barrier-forming claudins. Moreover, the ECS1 sequence of hCLDN4 and hCLDN3 share 94.2% identity and 100% similarity. Thus, sequence comparison fits perfectly with the ion barrier formation found in this study.

Cldn8 shows more positively charged residues in ECS1 than Cldn4 and thus—concerning the sequence—could support anion permeability better than Cldn4. However, the data showed that this is not the case.

One sequence difference between Cldn4 and Cldn3 of interest is the presence of a non-charged serine instead of a negatively charged glutamate in the ECS2 turn region of Cldn4. The corresponding position in Cldn10b and Cldn10a was suggested to be involved in charge selectivity of the respective ion channels.[64,65] Furthermore, this difference between Cldn3 and Cldn4 was proposed to be involved in their different capability to form TJ strands.[54] Thus, it is conceivable that the absence of a negative charge in the ECS2 turn contributes to the very week but measurable anion preference of Cldn4-containing TJ strands.

In conclusion, Cldn4 and Cldn19 act as barrier-forming claudins. Cldn2, -10b, -15 and -16 together with -19 are paracellular cation channels with differing preferences for mono- and divalent cations. Cldn10a is a paracellular anion channel with a preference of chloride over other anions. At acidic pH values in the absence of HCO_3^-, Cldn4 exhibits a slight preference for $NO_3^- > Cl^-$, but not for phosphate. Co-expression with Cldn8 abolishes this anion preference. Sequence data support the general ion

permeability and barrier properties identified for the claudins investigated in the present study.

4 | MATERIALS AND METHODS

4.1 | Cloning of dog *Cldn19b*

Specimens of dog kidney were purchased from KAC Co. Ltd. (Kyoto, Japan). Total RNA was isolated from the dog kidney using TRIzol™ Reagent (Thermo Fisher, Tokyo, Japan) and reverse-transcribed with SuperScript III Reverse Transcriptase (Thermo Fisher) to generate dog kidney cDNA library. Using this cDNA library as a template, dog Cldn19b from its 1st ATG to the stop codon were amplified by PCR with KOD-Plus-ver.2 DNA Polymerase (TOYOBO; Osaka, Japan) using a primer pair designed according to the dog genome sequence in Ensembl: ggggtcgacATGGCCAACTCGGGCCTCCAGC TCC (forward) and ggggaattcTCAGACGTACTCTCGG GCAGAGGC (reverse), and subcloned into pBlueScript SK(−) using the SalI and EcoRI restriction sites. After DNA sequencing, the dog Cldn19b cDNA was excised and subcloned into pCAGGS containing a neomycin-resistance gene,[66] to generate a dog Cldn19b expression vector.

4.2 | Subcloning of human *CLDN4* and *-8* cDNAs

Human *CLDN4* and *CLDN8* cDNAs were subcloned into pcDNA3-NECFP/-NEYFP (kindly provided by Otmar Huber, Friedrich Schiller University Jena, Jena, Germany) utilizing the BamHI and EcoRV restriction sites. This resulted in the linker sequence SLVPSSDP between the fluorescent protein and the N-terminus of the claudin.

4.3 | Cell line generation

Claudin quinKO cells and those stably expressing mouse Clnd2, -4, -8, -10a, -10b, -15, or dog Cldn16 were established and characterized as described previously.[33,42,67]

To establish claudin quinKO cells expressing dog Cldn19b, the plasmid DNA of the Cldn19b expression vector was transfected into claudin quinKO cells using Lipofectamine LTX Reagent with PLUS Reagent (Thermo Fisher Scientific GmbH, Dreieich, Germany). Cell colonies resistant to 300 μg/mL of G418 were picked up, followed by confirming the expression of Cldn19 immunofluorescence staining with anti-Cldn19 antibodies.[68] To establish claudin quinKO cells co-expressing Cldn19b and Cldn16,

a Cldn16 expression vector[33] and pGK-Puro, which contains a gene for puromycin-resistance, were co-transfected into a Cldn19b-expressing claudin quinKO cell clone. Cell colonies resistant to 300 μg/mL of G418 and 1.5 μg/mL of puromycin were picked, followed by confirmation of the expression of Cldn16 and Cldn19 by immunofluorescence staining. Claudin quinKO cells co-expressing Cldn4 and Cldn8 were established in the same manner from Cldn8-expressing claudin quinKO cell clone by co-transfection with a Cldn4 expression vector and pGK-Puro.

4.4 | Cell culture

All MDCK II-derived claudin quinKO cell lines were cultured with DMEM (high glucose and GlutaMax, Gibco, Thermo Fisher Scientific GmbH) supplemented with 10% (v/v) fetal bovine serum (Corning, NY, USA), 100 U/mL penicillin, and 100 μg/mL streptomycin (Sigma-Aldrich, Traufkirchen, Germany) at 37°C in a humidified 5% CO_2 atmosphere.

For claudin quinKO stably transfected with empty vector, mCldn2, mCldn4, mCldn8, mCldn10a, mCldn10b mCldn15, dCldn16, dCldn19 the medium additionally contained 300 μg/mL G418 (50 mg/mL, Carl Roth GmbH, Karlsruhe, Germany). Cells doubly transfected with mCldn4+8 or dCldn16+19 in addition to 300 μg/mL G418, received 1.5 μg/mL puromycin (Sigma-Aldrich).

For electrophysiological measurements and immunoblotting, 2×10^5 cells were seeded on polycarbonate membrane inserts (Millicell-PCF, pore size 0.4 μm, area 0.6 cm², Merck Millipore, Darmstadt, Germany) and were cultured for 7–8 days until stable resistance values were reached.

4.5 | Immunofluorescence staining

4.5.1 | Cldn4 and Cldn8

4×10^5 cells were plated on 0.4 μm polycarbonate Transwell filters (Corning, Corning, NY, USA; Cat. No. 3401) and cultured for 7 d. Cells on filters were fixed with 10% trichloroacetic acid (w/v in PBS) on ice for 30 min. After washing in PBS, cells were permeabilized in 0.2% Triton-X100 (Nacalai Tesque, Kyoto, Japan) in PBS for 15 min followed by 30 min blocking in 1% bovine serum albumin (Nacalai Tesque) in PBS. Cells were then incubated with primary antibodies (mCldn4 (Thermo Fisher Scientific, 32-9400) + rbCldn8,[69] ratOcln (MOC37)[70]) in a blocking solution for 30 min. After washing with PBS, cells were incubated with fluorescently labeled secondary antibodies for 30 min (donkey anti-rabbit Alexa Fluor 488, donkey anti-mouse Alexa Fluor

555, Thermo Fisher Scientific A21206 and A31570; Cy5-donkey anti-rat IgG; Jackson ImmunoResearch Laboratories 712-175-153, West Grove, PA, USA). Cells were again washed with PBS and mounted on slide glasses in FluorSave Reagent (Merck Millipore, Burlington, MA, USA) and covered with coverslips. Confocal images of cells were obtained using a confocal microscope (Model TCS SPE; Leica Microsystems, Wetzlar, Germany). Images were processed with Image J software (version 1.52k).

4.5.2 | Cldn16 and Cldn19

Cell layers grown either on filter membranes (Millicell) or on poly-lysin coated chambered glass-bottom slides (ibidi GmbH, Gräfelfing, Germany) were fixed in 10% trichloroacetic acid (Sigma-Aldrich; w/v in distilled water) on ice for 30 min. After washing in phosphate buffered solution (PBS; Gibco) cell layers were permeabilized in 0.5% Triton-X100 (Serva Electrophoresis GmbH, Heidelberg, Germany) in PBS followed by 30 min blocking in 1% bovine serum albumin (Serva Electrophoresis GmbH) in PBS. Cell layers were then incubated with primary antibodies (mCldn16[71] + rbCldn19[12]) in a blocking solution overnight. After washing, fluorescently labeled secondary antibodies were added (goat anti-rabbit Alexa Fluor 594; goat anti-mouse Alexa Fluor 647; Invitrogen-Thermo Fisher Scientific GmbH, A32740, and A32728) for 1 h. After further washing, directly labeled Alexa Fluor 488 mOcln (Invitrogen-Thermo Fisher Scientific GmbH, 331588) and DAPI (4′,6-diamidino-2-phenylindole dihydrochloride, stock 1 mg/mL methanol, 1:1000; Roche, Basel, Switzerland) were applied for 2 h. Cell layers were again washed and mounted in ProTaqs Mount Fluor (Biocyc GmbH, Potsdam, Germany) and imaged using a LSM 780 (Carl Zeiss Microscopy, Jena, Germany).

4.6 | Freeze-fracture electron microscopy

Stably transfected claudin quinKO cell layers grown on filter membranes were washed twice in PBS followed by fixation in 2.5% glutaraldehyde (Sigma-Aldrich) in PBS at room temperature for 2 h. After washing in PBS, cells were stored in 0.1% glutaraldehyde in PBS at 4°C until further processing. Cell layers were serially incubated in 10% (v/v; 30 min) followed by 30% glycerol in PBS (v/v; 30 min), followed by freezing in liquid nitrogen–cooled R422D (TEGA GmbH, Würzburg, Germany), mounted in a vacuum evaporator (Denton DV-502), fractured at −100°C, and shadowed with platinum and carbon. Cell debris was removed with sodium hypochlorite (Carl Roth, Karlsruhe, Germany) and the cleaned replicas were picked up on copper grids (Ted Pella Inc., Radding, CA), and analyzed with a Zeiss 902A electron microscope (Carl Zeiss AG; equipped with an Olympus iTEM Veleta video system).

4.7 | Life cell imaging, FRET assay

For analysis of the claudin cis-interaction by FRET assay, 2×10^5 claudin quinKO cells were seeded on poly-L-lysin (1:5 with H_2O, Sigma-Aldrich) coated glass coverslips. The next day, cells were co-transfected with 4 µg of different pairs of plasmid DNA (pcDNA3-NECFP/-NEYFP) encoding for YFP- and CFP- fusions of hCLDN4 or-hCLDN8, using 10 µL Lipofectamine 2000 (Invitrogen, Thermo Fisher Scientific GmbH). Three days after transfection, coverslips were transferred into HEPES-buffered solution (134.6 mM NaCl, 2.4 mM Na_2HPO_4, 0.6 mM NaH_2PO_4, 5.4 mM KCl, 1.2 mM $CaCl_2$, 1 mM $MgSO_4$, 10 mM HEPES, 25 mM D(+)-glucose, pH 7.4) and analyzed using a Zeiss LSM 780 at 37°C. FRET assay was performed and analyzed at cell–cell contacts as described previously for HEK293 and MDCKII cells.[50,52,72] Briefly, the FRET efficiency (EF) was calculated as the relative increase in CFP fluorescence intensity before (Ib) and after (Ia) acceptor bleach (EF = (Ia − Ib)/Ia × 100). Measurements were carried out at different YFP/CFP ratios. Signals were calibrated using a YFP/CFP tandem protein so that equal YFP and CFP intensities denote equal protein amounts. EF values were plotted against the corresponding YFP-claudin/CFP-claudin ratio to test for the dependence on the FRET acceptor/donor ratio and/or the CLDN4/CLDN8 ratio.

4.8 | Western blots

Cells grown on filter inserts were lysed in 120 µL RIPA buffer (25 mM Tris–HCl, pH 7.6, 150 mM NaCl, 1% NP-40, 1% sodium deoxycholate, 0.1% SDS) supplemented with EDTA-free protease inhibitor cocktail (cOmplete™ EDTA free; Roche) and phosphatase inhibitor (Roche). Cells were scraped from the filter membrane and incubated on ice for 1–1.5 h, vortexing every 10–15 min. After sonication samples were centrifuged at 4°C, 15 000 rpm for 15 min and the supernatant was collected. Protein concentration was determined with a Pierce bicinchoninic acid protein assay (Thermo Fisher Scientific GmbH). 20 µg of protein per sample were mixed with Laemmli buffer, heated to 95°C for 5 min, separated on a 12.5% polyacrylamide gel, and transferred onto a polyvinylidene difluoride (PVDF, Thermo Fisher Scientific GmbH) membrane. The membrane was cut just below the 36 kDa marker

band, blocked with 1% PVP-40, 0.05% Tween-20 in H_2O for 60 min and the upper part probed with a m-β-actin antibody (1:10 000; Clone AC-15, A5441, Sigma—Aldrich), the lower part with a m-Cldn4 (1:5000; 32-9400, Thermo Fisher Scientific GmbH), rb-Cldn8 (1:1000; 40-0700Z, Thermo Fisher Scientific GmbH), or rb-phospho-tyrosine-208-Cldn4 (1: 2000; PA5-118685, Thermo Fisher Scientific GmbH) antibody, respectively. Immunodetection was performed employing HRP-conjugated secondary antibodies (1:10 000; Jackson ImmunoResearch, West Grove, PA, USA) and SuperSignal West Pico Plus (ThermoFisher Scientific GmbH). Signals were visualized by the Fusion FX6 chemiluminescence imaging system (Vilber Lourmat Deutschland GmbH, Eberhardzell, Germany).

4.9 | Ussing chamber experiments

4.9.1 | Solutions

Composition of all solutions used in the Ussing chamber experiments is listed in Table S2.

4.9.2 | Fluorescein permeability

P_{Fluo} was calculated from flux measurements performed in Ussing chambers. Briefly, fluorescein (fluorescein sodium salt; Sigma-Aldrich) was added to the apical hemi-chamber (donor side) at a final concentration of 100 μM. Samples were collected from the basolateral side immediately after apical application (=t0) and then 5, 10, and 15 min (high permeability cell layers) or 10, 20, and 30 min after t0 (low permeability cell layers), and immediately replaced with fresh solution. Samples were measured in duplicates, using a plate reader (Infinite M200, Tecan GmbH, Männedorf, Switzerland). Fluorescence concentrations were calculated according to a calibration curve. Flux was calculated as the increase in fluorescein concentration (corrected for dilution) per time and filter area (0.6 cm^2). P_{Fluo} was calculated as the ratio of flux and concentration on the donor side.

4.9.3 | Dilution and bi-ionic potential measurements

Dilution and bi-ionic potential measurements were essentially carried out and permeabilities were calculated as previously described in great detail.[25] In brief, filter inserts were mounted in Ussing chambers and equilibrated in the appropriate NaCl-based solution (solution #1 to 4;

Table S3). Half of the apical solution was replaced by the appropriate Mannitol-based solution (#5 to 8; Table S3) and the measured voltage deflection liquid junction potential (LJP) was corrected and used to calculate P_{Na}/P_{Cl} using the Goldman equation. Subsequently, half of the basolateral solution was replaced by the appropriate test solutions (#9–14 for anion permeabilities, #15–18 for monovalent cation permeabilities, #19–22 for ammonium-derived cations, #23–26 for divalent cations; Table S3). Relative permeabilities were calculated from the resulting, LJP-corrected potential deflections using the Goldman equation, and the P_{Na}/P_{Cl} was determined for the same filter insert (for equations, see Ref. [25]). Absolute permeabilities were calculated using the Kimizuka-Koketsu equation (Ref. [44]; eq. 2 in Ref. [25]).

4.10 | Statistics

Statistical calculations were carried out with Graphpad/Prism version 9.4.0(673) (San Diego, CA, USA). For data shown in Figures 1 and 8, a Brown-Forsythe and Welch ANOVA followed by a Dunnet's T3 multiple comparisons test was applied, to allow for different variances between the groups. Otherwise, a Students t-test was applied, if only two groups were compared, or an ordinary one-way ANOVA and Dunnet's T3 multiple comparisons test for comparisons of two or more groups to a shared control group.

AUTHOR CONTRIBUTIONS
Ioanna Pouyiourou: Investigation; formal analysis; visualization; writing – original draft. **Anja Fromm:** Investigation; writing – review and editing. **Jörg Piontek:** Visualization; writing – review and editing; methodology. **Rita Rosenthal:** Formal analysis; visualization; writing – review and editing. **Mikio Furuse:** Conceptualization; investigation; funding acquisition; visualization; writing – review and editing. **Dorothee Günzel:** Conceptualization; investigation; visualization; writing – original draft; formal analysis; funding acquisition.

CONFLICT OF INTEREST STATEMENT

The authors declare no conflicts of interest.

DATA AVAILABILITY STATEMENT

The data that support the findings of this study are available from the corresponding author upon reasonable request.

ORCID

Ioanna Pouyiourou https://orcid.org/0009-0005-0403-8852
Anja Fromm https://orcid.org/0000-0003-4091-9612
Jörg Piontek https://orcid.org/0000-0002-0880-8915
Rita Rosenthal https://orcid.org/0000-0002-5807-9415
Mikio Furuse https://orcid.org/0000-0003-2847-8156
Dorothee Günzel https://orcid.org/0000-0002-7998-7164

REFERENCES

1. Günzel D, Yu AS. Claudins and the modulation of tight junction permeability. *Physiol Rev*. 2013;93(2):525-569.
2. Meoli L, Günzel D. The role of claudins in homeostasis. *Nat Rev Nephrol*. 2023;19(9):587-603.
3. Kirk A, Campbell S, Bass P, Mason J, Collins J. Differential expression of claudin tight junction proteins in the human cortical nephron. *Nephrol Dial Transplant*. 2010;25(7):2107-2119.
4. Kiuchi-Saishin Y, Gotoh S, Furuse M, Takasuga A, Tano Y, Tsukita S. Differential expression patterns of claudins, tight junction membrane proteins, in mouse nephron segments. *J Am Soc Nephrol*. 2002;13(4):875-886.
5. Reyes JL, Lamas M, Martin D, et al. The renal segmental distribution of claudins changes with development. *Kidney Int*. 2002;62(2):476-487.
6. Chen L, Chou CL, Knepper MA. A comprehensive map of mRNAs and their isoforms across all 14 renal tubule segments of mouse. *J Am Soc Nephrol*. 2021;32(4):897-912.
7. Ransick A, Lindstrom NO, Liu J, et al. Single-cell profiling reveals sex, lineage, and regional diversity in the mouse kidney. *Dev Cell*. 2019;51(3):399-413.e7.
8. Tesch F, Siegerist F, Hay E, et al. Super-resolved local recruitment of CLDN5 to filtration slits implicates a direct relationship with podocyte foot process effacement. *J Cell Mol Med*. 2021;25(16):7631-7641.
9. Tsamo Tetou A, Günzel D. The role of claudins in renal transepithelial transport and kidney disease. *Curr Opin Nephrol Hypertens*. 2024;33:535-542.
10. Dimke H, Desai P, Borovac J, Lau A, Pan W, Alexander RT. Activation of the Ca(2+)-sensing receptor increases renal claudin-14 expression and urinary Ca(2+) excretion. *Am J Physiol Renal Physiol*. 2013;304(6):F761-F769.
11. Frische S, Alexander RT, Ferreira P, et al. Localization and regulation of claudin-14 in experimental models of hypercalcemia. *Am J Physiol Renal Physiol*. 2021;320(1):F74-F86.
12. Gong Y, Renigunta V, Himmerkus N, et al. Claudin-14 regulates renal Ca^{++} transport in response to CaSR signalling via a novel microRNA pathway. *EMBO J*. 2012;31(8):1999-2012.
13. Liu WB, Huang GR, Liu BL, et al. Single cell landscape of parietal epithelial cells in healthy and diseased states. *Kidney Int*. 2023;104(1):108-123.
14. Dumas SJ, Meta E, Borri M, et al. Single-cell RNA sequencing reveals renal endothelium heterogeneity and metabolic adaptation to water deprivation. *J Am Soc Nephrol*. 2020;31(1):118-138.
15. Angelow S, Yu AS. Claudins and paracellular transport: an update. *Curr Opin Nephrol Hypertens*. 2007;16(5):459-464.
16. Ben-Yosef T, Belyantseva IA, Saunders TL, et al. Claudin 14 knockout mice, a model for autosomal recessive deafness DFNB29, are deaf due to cochlear hair cell degeneration. *Hum Mol Genet*. 2003;12(16):2049-2061.
17. Furuse M, Hata M, Furuse K, et al. Claudin-based tight junctions are crucial for the mammalian epidermal barrier: a lesson from claudin-1-deficient mice. *J Cell Biol*. 2002;156(6):1099-1111.
18. Inai T, Kobayashi J, Shibata Y. Claudin-1 contributes to the epithelial barrier function in MDCK cells. *Eur J Cell Biol*. 1999;78(12):849-855.
19. Milatz S, Krug SM, Rosenthal R, et al. Claudin-3 acts as a sealing component of the tight junction for ions of either charge and uncharged solutes. *Biochim Biophys Acta*. 2010;1798(11):2048-2057.
20. Nitta T, Hata M, Gotoh S, et al. Size-selective loosening of the blood-brain barrier in claudin-5–deficient mice. *J Cell Biol*. 2003;161(3):653-660.
21. Wen H, Watry DD, Marcondes MC, Fox HS. Selective decrease in paracellular conductance of tight junctions: role of the first extracellular domain of claudin-5. *Mol Cell Biol*. 2004;24(19):8408-8417.
22. Breiderhoff T, Himmerkus N, Meoli L, et al. Claudin-10a deficiency shifts proximal tubular Cl(−) permeability to cation selectivity via claudin-2 redistribution. *J Am Soc Nephrol*. 2022;33(4):699-717.
23. Van Itallie CM, Rogan S, Yu A, Vidal LS, Holmes J, Anderson JM. Two splice variants of claudin-10 in the kidney create paracellular pores with different ion selectivities. *Am J Physiol Renal Physiol*. 2006;291(6):1288-1299.
24. Amasheh S, Meiri N, Gitter AH, et al. Claudin-2 expression induces cation-selective channels in tight junctions of epithelial cells. *J Cell Sci*. 2002;115:4969-4976.
25. Günzel D, Stuiver M, Kausalya PJ, et al. Claudin-10 exists in six alternatively spliced isoforms that exhibit distinct localization and function. *J Cell Sci*. 2009;122(10):1507-1517.
26. Beggs MR, Young K, Pan W, et al. Claudin-2 and claudin-12 form independent, complementary pores required to maintain calcium homeostasis. *Proc Natl Acad Sci U S A*. 2021;118(48):e2111247118.
27. Fujita H, Sugimoto K, Inatomi S, et al. Tight junction proteins claudin-2 and -12 are critical for vitamin D-dependent Ca^{2+} absorption between enterocytes. *Mol Biol Cell*. 2008;19(5):1912-1921.

28. Colegio OR, Van Itallie CM, McCrea HJ, Rahner C, Anderson JM. Claudins create charge-selective channels in the paracellular pathway between epithelial cells. *Am J Physiol Cell Physiol*. 2002;283(1):142-147.

29. Hou JH, Renigunta A, Gomes AS, et al. Claudin-16 and claudin-19 interaction is required for their assembly into tight junctions and for renal reabsorption of magnesium. *Proc Natl Acad Sci U S A*. 2009;106(36):15350-15355.

30. Hou JH, Renigunta A, Konrad M, et al. Claudin-16 and claudin-19 interact and form a cation-selective tight junction complex. *J Clin Invest*. 2008;118(2):619-628.

31. Alexandre MD, Lu Q, Chen YH. Overexpression of claudin-7 decreases the paracellular Cl⁻ conductance and increases the paracellular Na⁺ conductance in LLC-PK1 cells. *J Cell Sci*. 2005;118:2683-2693.

32. Amasheh S, Milatz S, Krug SM, et al. Na⁺ absorption defends from paracellular back-leakage by claudin-8 upregulation. *Biochem Biophys Res Commun*. 2009;378(1):45-50.

33. Furuse M, Nakatsu D, Hempstock W, et al. Reconstitution of functional tight junctions with individual claudin subtypes in epithelial cells. *Cell Struct Funct*. 2023;48(1):1-17.

34. Jeansonne B, Lu Q, Goodenough DA, Chen YH. Claudin-8 interacts with multi-PDZ domain protein 1 (MUPP1) and reduces paracellular conductance in epithelial cells. *Cell Mol Biol (Noisy-le-Grand)*. 2003;49(1):13-21.

35. Van Itallie C, Rahner C, Anderson JM. Regulated expression of claudin-4 decreases paracellular conductance through a selective decrease in sodium permeability. *J Clin Invest*. 2001;107(10):1319-1327.

36. D'Souza T, Indig FE, Morin PJ. Phosphorylation of claudin-4 by PKCepsilon regulates tight junction barrier function in ovarian cancer cells. *Exp Cell Res*. 2007;313(15):3364-3375.

37. Hou J, Gomes AS, Paul DL, Goodenough DA. Study of claudin function by RNA interference. *J Biol Chem*. 2006;281(47):36117-36123.

38. Hou J, Renigunta A, Yang J, Waldegger S. Claudin-4 forms paracellular chloride channel in the kidney and requires claudin-8 for tight junction localization. *Proc Natl Acad Sci U S A*. 2010;107(42):18010-18015.

39. Le Moellic C, Boulkroun S, Gonzalez-Nunez D, et al. Aldosterone and tight junctions: modulation of claudin-4 phosphorylation in renal collecting duct cells. *Am J Physiol Cell Physiol*. 2005;289(6):C1513-C1521.

40. Tatum R, Zhang YG, Salleng K, et al. Renal salt wasting and chronic dehydration in claudin-7-deficient mice. *Am J Physiol Renal Physiol*. 2010;298(1):F24-F34.

41. Angelow S, Schneeberger EE, Yu AS. Claudin-8 expression in renal epithelial cells augments the paracellular barrier by replacing endogenous claudin-2. *J Membr Biol*. 2007;215(2–3):147-159.

42. Otani T, Nguyen TP, Tokuda S, et al. Claudins and JAM-A coordinately regulate tight junction formation and epithelial polarity. *J Cell Biol*. 2019;218(10):3372-3396.

43. Hou J, Paul DL, Goodenough DA. Paracellin-1 and the modulation of ion selectivity of tight junctions. *J Cell Sci*. 2005;118:5109-5118.

44. Kimizuka H, Koketsu K. Ion transport through cell membrane. *J Theor Biol*. 1964;6(2):290-305.

45. Diamond JM, Wright EM. Biological membranes: the physical basis of ion and nonelectrolyte selectivity. *Annu Rev Physiol*. 1969;31:581-646.

46. Yu ASL, Cheng MH, Angelow S, et al. Molecular basis for cation selectivity in claudin-2-based paracellular pores: identification of an electrostatic interaction site. *J Gen Physiol*. 2009;133(1):111-127.

47. Renkin EM. Filtration, diffusion, and molecular sieving through porous cellulose membranes. *J Gen Physiol*. 1954;38(2):225-243.

48. Nightingale ER. Phenomenological theory of ion solvation. Effective radii of hydrated ions. *J Phys Chem*. 1959;63:1381-1387.

49. Villarroel A, Burnashev N, Sakmann B. Dimensions of the narrow portion of a recombinant NMDA receptor-channel. *Biophys J*. 1995;68(3):866-875.

50. Milatz S, Piontek J, Schulzke JD, Blasig IE, Fromm M, Günzel D. Probing the cis-arrangement of prototype tight junction proteins claudin-1 and claudin-3. *Biochem J*. 2015;468(3):449-458.

51. Gonschior H, Schmied C, Van der Veen RE, et al. Nanoscale segregation of channel and barrier claudins enables paracellular ion flux. *Nat Commun*. 2022;13(1):4985.

52. Milatz S, Piontek J, Hempel C, et al. Tight junction strand formation by claudin-10 isoforms and claudin-10a/-10b chimeras. *Ann N Y Acad Sci*. 2017;1405(1):102-115.

53. Shashikanth N, France MM, Xiao R, et al. Tight junction channel regulation by interclaudin interference. *Nat Commun*. 2022;13(1):3780.

54. van der Veen R, Piontek J, Bieck M, Saiti A, Gonschior H, Lehmann M. Claudin-4 polymerizes after the incorporation of just two extracellular claudin-3 residues. *bioRxiv* 2023, Preprint. doi:10.1101/2023.12.15.571691

55. Weinstein AM. A mathematical model of distal nephron acidification: diuretic effects. *Am J Physiol Renal Physiol*. 2008;295(5):F1353-F1364.

56. Qu XM, Wu ZF, Pang BX, Jin LY, Qin LZ, Wang SL. From nitrate to nitric oxide: the role of salivary glands and oral bacteria. *J Dent Res*. 2016;95(13):1452-1456.

57. Abd El-Ghani SF, Kasem RF, Ghallab NA, Shaker OG. Detection of claudin-4 in salivary gland neoplasms (a study utilizing RT-PCR and immunohistochemistry). *J Oral Pathol Med*. 2013;42(10):781-787.

58. Sassi A, Wang YB, Chassot A, et al. Expression of claudin-8 is induced by aldosterone in renal collecting duct principal cells. *Am J Physiol Renal Physiol*. 2021;321(5):F645-F655.

59. Hempel C, Protze J, Altun E, et al. Assembly of tight junction strands: claudin-10b and claudin-3 form homo-tetrameric building blocks that polymerise in a channel-independent manner. *J Mol Biol*. 2020;432(7):2405-2427.

60. Simon DB, Lu Y, Choate KA, et al. Paracellin-1, a renal tight junction protein required for paracellular Mg²⁺ resorption. *Science*. 1999;285(5424):103-106.

61. Konrad M, Schaller A, Seelow D, et al. Mutations in the tight-junction gene claudin 19 (CLDN19) are associated with renal magnesium wasting, renal failure, and severe ocular involvement. *Am J Hum Genet*. 2006;79(5):949-957.

62. Hempel C, Rosenthal R, Fromm A, et al. Tight junction channels claudin-10b and claudin-15: functional mapping of pore-lining residues. *Ann N Y Acad Sci*. 2022;1515(1):129-142.

63. Piontek J, Krug SM, Protze J, Krause G, Fromm M. Molecular architecture and assembly of the tight junction backbone. *Biochim Biophys Acta Biomembr*. 2020;1862(7):183279.

64. Nagarajan SK, Piontek J. Molecular dynamics simulations of claudin-10a and -10b ion channels: with similar architecture,

different pore linings determine the opposite charge selectivity. *Int J Mol Sci.* 2024;25(6):3161.

65. Nagarajan SK, Klein S, Fadakar BS, Piontek J. Claudin-10b cation channels in tight junction strands: Octameric-interlocked pore barrels constitute paracellular channels with low water permeability. *Comput Struct Biotechnol J.* 2023;21:1711-1727.

66. Niwa H, Yamamura K, Miyazaki J. Efficient selection for high-expression transfectants with a novel eukaryotic vector. *Gene.* 1991;108(2):193-199.

67. Alija C, Knobe L, Pouyiourou I, Furuse M, Rosenthal R, Günzel D. Integrating continuous transepithelial flux measurements into an Ussing chamber set-up. *Int J Mol Sci.* 2024;25(4):2252.

68. Miyamoto T, Morita K, Takemoto D, et al. Tight junctions in Schwann cells of peripheral myelinated axons: a lesson from claudin-19-deficient mice. *J Cell Biol.* 2005;169(3):527-538.

69. Morita K, Furuse M, Fujimoto K, Tsukita S. Claudin multigene family encoding four-transmembrane domain protein components of tight junction strands. *Proc Natl Acad Sci U S A.* 1999;96(2):511-516.

70. Saitou M, Ando-Akatsuka Y, Itoh M, et al. Mammalian occludin in epithelial cells: its expression and subcellular distribution. *Eur J Cell Biol.* 1997;73(3):222-231.

71. Prot-Bertoye C, Griveau C, Skjodt K, et al. Differential localization patterns of claudin 10, 16, and 19 in human, mouse, and rat renal tubular epithelia. *Am J Physiol Renal Physiol.* 2021;321(2):F207-F224.

72. Klar J, Piontek J, Milatz S, et al. Altered paracellular cation permeability due to a rare CLDN10B variant causes anhidrosis and kidney damage. *PLoS Genet.* 2017;13(7):e1006897.

SUPPORTING INFORMATION

Additional supporting information can be found online in the Supporting Information section at the end of this article.